Front. Mech. Eng. 2025, 20(6): 53
https://doi.org/10.1007/s11465-025-0869-8

RESEARCH ARTICLE

Performance analysis and optimization of aerostatic bearings with arrayed multi-orifice restrictors

Yifan ZHOU[1,2], Jiulin WU[1,2], Puliang YU[3], Xuedong CHEN[1,2], Wei JIANG (✉)[1,2]

[1] State Key Laboratory of Intelligent Manufacturing Equipment and Technology, Huazhong University of Science and Technology, Wuhan 430074, China
[2] School of Mechanical Science and Engineering, Huazhong University of Science and Technology, Wuhan 430074, China
[3] Key Laboratory of Metallurgical Equipment and Control Technology (Ministry of Education), Wuhan University of Science and Technology, Wuhan 430081, China

✉ Corresponding author. Email: jiangw@hust.edu.cn (Wei JIANG)

ABSTRACT Aerostatic bearings are extensively utilized in applications such as semiconductor processing and ultraprecision machining. However, turbulence in the bearing recess induces micro-vibration, which significantly affects stability. This study proposes an innovative arrayed multi-orifice restrictor (AMR) with square or circular distribution to limit the generation of turbulence and diminish bearing micro-vibration. The steady air flow field properties and static performance of bearings with square and circular AMRs are compared under various AMR geometric parameters through computational fluid dynamics. Through three-dimensional large eddy simulation, the transient flow properties of the flow field and pressure fluctuations of the bearings with AMRs are analyzed. This analysis clarifies the influence of the array number, spacing, and distribution types on the suppression of turbulent vortex occurrence and vibration amplitude. Results demonstrate that the optimized design of AMR significantly suppresses the generation of turbulent vortices, which makes the airflow entering the recess more uniform and orderly. Consequently, the vibration amplitude of bearings can be reduced effectively without sacrificing the load-carrying capacity and stiffness. Bearings with circular AMR have better stability and weaker vibration amplitude than those with square AMR.

Keywords aerostatic bearing, arrayed multi-orifice restrictor, turbulence, large eddy simulation, vibration

1 Introduction

Aerostatic bearings are extensively utilized in diverse domains, including semiconductor processing [1–3], ultra-precision machining [4,5], and spacecraft simulators [6,7], due to their near-zero friction, pollution-free operation, and superior precision. The efficacy of aerostatic bearings is primarily influenced by the type of restrictors, with orifice and porous being two common structural configurations [8–11]. Porous aerostatic bearings exhibit a remarkably uniform pressure distribution across the bearing surface and demonstrate high stability [12,13]. However, impurities in the air supply can quickly clog the complex pore structure of porous materials, which directly affects the performance and service life of the bearings [14–17]. The orifice restrictors have a simple structure and are easy to manufacture. Compared with aerostatic bearings without recesses, those with recesses demonstrate higher load-carrying capacity (LCC) and stiffness, which make them more widely applicable [18,19]. Further improving the static performance and the stability of aerostatic bearings with recesses is required with increasing requirement for the machining accuracy in ultra-precision machining equipment.

Researchers have devoted great efforts on the properties of aerostatic bearings with recesses, including LCC, stiffness, and pressure distribution. Boffey et al. [20,21] experimentally examined the effect of orifice size on the performance of bearings. Li and Ding [22] developed a simplified approach to analyze the influence of factors such as film thickness, air properties, and structural parameters on the performance of

Received February 28, 2025; accepted July 3, 2025; online December 25, 2025

aerostatic bearings. Charki et al. [23] evaluated the stiffness and damping characteristics of aerostatic bearings with multiple orifices through finite element modeling and the nonlinear Reynolds equation. Wen et al. [24] proposed a mesh refinement approach for multi-hole aerostatic bearings and investigated the impact of recess structure parameters on carrying capacity. Wang et al. [25,26] demonstrated that the relationship between the inherent frequency in the load system and the frequency of pressure variation in the flow field determines the pneumatic hammer phenomena through theoretical research. They also proposed a novel aerostatic bearing design with hermetically squeeze film dampers to improve the stability by enhancing viscous damping and stiffness under various operating conditions. Zhou et al. [27] developed a hybrid approach that combines the Navier–Stokes (N-S) equations and Reynolds equations. This approach improves accuracy and efficiency in simulating the air flow of aerostatic bearings. Li and Ding [28] investigated the LCC and stiffness of bearings with different structural parameters and validated the simulation results through several experiments. The findings indicated that enlarging the pocket geometrical dimensions enhances the static performance of bearings. However, this setting also causes the air velocity to rise, which potentially reaches supersonic speeds. This condition negatively impacts the stability of the bearing. Du et al. [29] opened grooves to enhance the LCC and stiffness of bearings. However, this method may adversely affect the surface quality of the bearing, which is essential to preserving the motion stability. Zheng et al. [30] proposed a new type of restrictor that consists of several holes connected in sequence to increase peak stiffness, but the LCC of bearing decreases. Chen and He [31] examined the influence of the recessed shape on effectiveness analysis using numerical methods. Among bearings of different shapes (non-pocketed, square recessed, and spherical recessed), the square recessed bearing exhibits the highest LCC. They discovered the vortex phenomenon in the recess, which could lead to micro-vibrations. Zhu et al. [32] investigated vortex shedding phenomena in the recess. The results showed that pressure fluctuations induced by turbulent vortices can lead to micro-vibrations and cause bearing instability.

Many researchers have studied the dynamic performance of aerostatic bearings to mitigate vortex and improve stability. Aoyama et al. [33] performed a detailed numerical simulation of the flow field in aerostatic bearings. Their findings indicated that the rounded corner optimization of the restrictor outlet improves the stability of the airflow in the tolerance of the bearing by efficiently reducing vortex formation. Ma et al. [34] used numerical calculation methods to examine the dynamic properties of the aerostatic bearings. According to their investigation, the implementation of a damping orifice significantly reduces the occurrence of pneumatic hammer. Subsequently, Aoyama et al. [35] introduced a cross-groove design to mitigate the pressure rise associated with small pores. This design has proven effective in reducing micro-bounce motion. Chen et al. [36] proposed using an appropriate number of orifices instead of a single restrictor to enhance the stability of bearings. The findings indicated that the application of orifice design can inhibit the creation of vortices in the recess, which improves the bearing stability while preserving the static characteristics. Feng et al. [37] used 3D printing technology to fabricate four types of restrictor structures and analyzed static characteristics and pressure fluctuation. Their study demonstrated that the arc-hole restrictor can reduce the pressure fluctuations in the flow field. Li et al. [38,39] introduced an innovative aerostatic bearing featuring a passage for backflow, which connects the recess and the lower pressure area of the air film. Their results demonstrated that this design simultaneously enhances the performance of bearings. Yu et al. [40] presented a restrictor with inclined holes and analyzed the flow field characteristics to optimize the angle of the inclined holes. This restrictor suppresses turbulence formation and reduces micro-vibrations. Zhao et al. [41] applied proper orthogonal decomposition and large eddy simulation (LES) to analyze flow characteristics in aerostatic bearings. The results revealed that supply pressure and film thickness influence the vortex structures and micro-vibration suppression. Li et al. [42] investigated novel active aerostatic bearings with controllable throttling effects. They demonstrated through numerical and experimental studies that active flow resistance compensation enhances static stiffness and suppresses vortices compared with passive designs. Yu et al. [43] proposed a new type of five-hole restrictor for aerostatic bearings. Their findings showed that optimizing the secondary orifice diameter can improve LCC and reduce nano-vibrations. Therefore, optimizing the structural design of the restrictor effectively suppresses turbulence formation, which reduces micro-vibrations of bearings.

Researchers have given considerable attention to enhancing the stability of bearings with recesses. Altering recess structures, regulating supply pressure, and adjusting bearing parameters can mitigate vortex effects. However, these approaches do not fully eliminate the presence of vortices. Drawing from the examination of the turbulence vortex production mechanism, this study introduces a novel aerostatic bearing design with a square or circular arrayed multi-orifice restrictor (AMR) to improve the dynamic

performance of aerostatic bearings. The pressure distribution, static performances, and the flow field properties of bearings with various array numbers, spacing, and distribution types are compared and analyzed. Three-dimensional LES is utilized to obtain the pressure fluctuations and the dynamic behavior of the airflow in the aerostatic bearing. Accordingly, the influence of the array number, spacing, and distribution on turbulent vortices in the recess and the stability of bearing is clarified. This research aims to provide a novel approach for inhibiting the creation of vortices, decreasing micro-vibrations, and improving the stability of the bearing.

2 Geometrical and numerical models

2.1 Geometrical model

For the 1-orifice aerostatic bearing, as the orifice diameter decreases, the turbulence intensity in the recess diminishes. This decline significantly diminishes the micro-vibrations of bearing. However, it results in a reduction in pressure in the flow field, which subsequently decreases the bearing LCC. To address this contradiction, an innovative design of an aerostatic bearing with square or circular AMRs is proposed. Figure 1 shows the structure diagram of the aerostatic bearings with different AMRs. The restrictor uses arrayed multi-orifices instead of the traditional single orifice. This design achieves the goal of reducing micro-vibrations in the aerostatic bearing by inhibiting the generation of turbulent vortices while maintaining the LCC. With the total restricted area of the structure remaining constant, a greater number of arrayed multi-orifices result in a smaller multi-orifice diameter. The advantage of this design is that the smaller orifice diameter can effectively inhibit the generation of turbulent vortex structures, while the increased numbers of multi-orifices guarantee that the restrictor area stays unchanged. In this way, the stiffness and LCC of bearings are unaffected. The structure parameters of the bearings with AMRs are shown in Table 1.

The orifices are fabricated by laser-drilling ruby discs, which are embedded in the recess. Notably, d_o is the diameter of the ruby disc. Considering that the size of orifices varies with the number of multi-orifices, the spacing l is defined as the distance between the edges of two neighboring orifices along the diagonal of the square AMR. Figures 1(c) and 1(d) show the square AMR with 16 and 36 orifices, while Figs. 1(e) and 1(f) show the circular AMR with 16 and 36 orifices. As shown in Figs. 1(e) and 1(f), to clearly illustrate the positional changes in the orifices caused by the change from square to circular distribu-

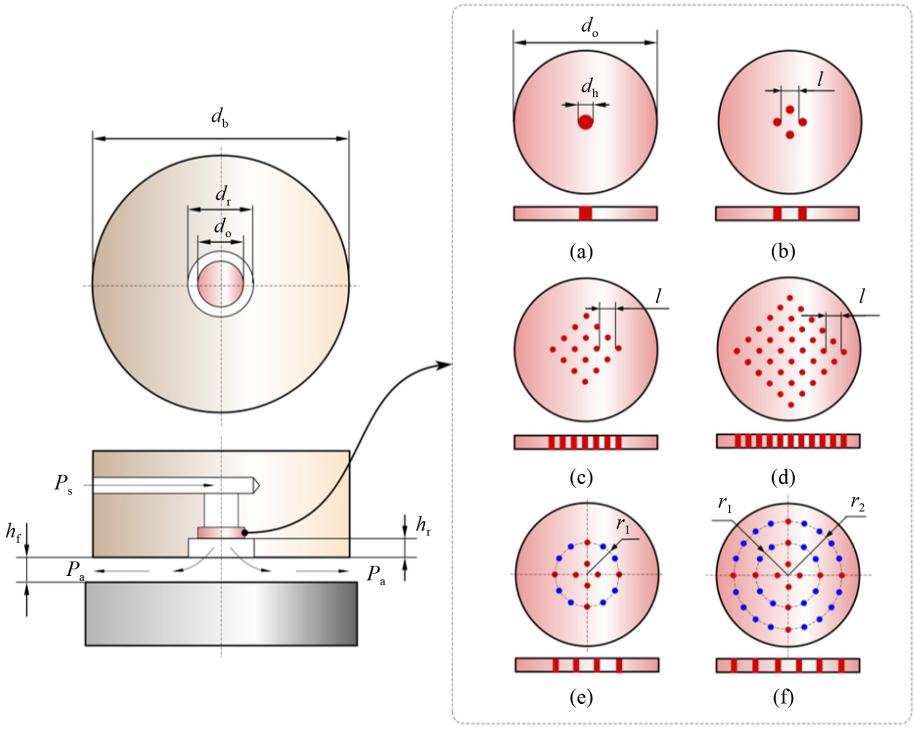

Fig. 1 Bearing structure with different AMRs: (a) 1-orifice AMR, $n = 1$; (b) square AMR, $n = 4$; (c) square AMR, $n = 16$; (d) square AMR, $n = 36$; (e) circular AMR, $n = 16$; (f) circular AMR, $n = 36$. The structure parameters are listed in Table 1.

Table 1 Structure parameters of bearings with AMRs

Parameters	Symbol	Value				Unit
Number of multi-orifices	n	1	4	16	36	–
Diameter of the orifice	d_{h}	0.3	0.15	0.075	0.05	mm
Spacing of orifices	l	0.2/0.3/0.4[a)]				mm
Diameter of the recess	d_{r}	3				mm
Depth of the recess	h_{r}	0.1				mm
Diameter of the bearing	d_{b}	15				mm
Gas film thickness	h_{f}	10				μm
External supply pressure	P_{s}	0.4				MPa
Atmosphere pressure	P_{a}	0.1				MPa

a) These parameters do not apply to the case when $n = 1$.

tion, the orifices shown in blue indicate those whose positions have shifted relative to the original square distribution. By contrast, the orifices located along the diagonals of the square distribution remain unchanged and are still marked in red. In the circular AMR with 16 orifices, the outer ring of multi-orifices is evenly distributed along a circle with a radius of r_1, where $r_1 = 1.5(l + d_{\mathrm{h}})$. Similarly, in the circular AMR with 36 orifices, the outermost orifices are evenly distributed along a circle with a radius of r_2, where $r_2 = 2.5(l + d_{\mathrm{h}})$, and the second outer ring of multi-orifices is distributed along a circle with a radius of r_1.

2.2 Numerical model

LES ensures the accuracy of turbulence resolution with relatively lower computational costs and is widely used in simulating the instantaneous flow field of bearings. The compressible N-S equations are filtered using a density-weighted filtering method (Favre filtering) to obtain the compressible LES governing equations [30,38], including the continuity, momentum, and energy equations:

$$\frac{\partial \bar{\rho}}{\partial t} + \frac{\partial(\bar{\rho}\tilde{u}_i)}{\partial x_i} = 0, \tag{1}$$

$$\frac{\partial(\bar{\rho}\tilde{u}_i)}{\partial t} + \frac{\partial(\bar{\rho}\tilde{u}_i\tilde{u}_j)}{\partial x_j} = -\frac{\partial \bar{p}}{\partial x_i} + \frac{\partial \tilde{\sigma}_{ij}}{\partial x_j} - \frac{\partial \tilde{\tau}_{ij}}{\partial x_j}, \tag{2}$$

$$\frac{\partial(\bar{\rho}\tilde{E})}{\partial t} + \frac{\partial[(\bar{\rho}\tilde{E} + \bar{p})\tilde{u}_j]}{\partial x_j} = \frac{\partial(\sigma_{ij}\tilde{u}_i)}{\partial x_j} + \frac{\partial q_j}{\partial x_j} + \frac{\partial q_j^{\mathrm{SGS}}}{\partial x_j}, \tag{3}$$

where density ρ and pressure P are subjected to conventional physical space filtering (represented by the overscript "$-$"), while velocity u_i and velocity u_j are subjected to the density-weighted filtering (represented by the overscript "$\sim$"), q_j^{SGS} represents the subgrid-scale (SGS) heat flux, and $\tilde{\sigma}_{ij}$ is the filtered molecular viscous stress tensors:

$$\sigma_{ij} = \mu\left(\frac{\partial \tilde{u}_i}{\partial x_j} + \frac{\partial \tilde{u}_j}{\partial x_i} - \frac{2}{3}\delta_{ij}\frac{\partial \tilde{u}_k}{\partial x_k}\right). \tag{4}$$

The SGS stress $\tilde{\tau}_{ij}$ is defined as

$$\tau_{ij} = \frac{1}{3}\tau_{kk}\delta_{ij} - 2\,\mu_{\mathrm{SGS}}\,\bar{S}_{ij}, \tag{5}$$

$$\bar{S}_{ij} = \frac{1}{2}\left(\frac{\partial \bar{u}_i}{\partial x_j} + \frac{\partial \bar{u}_j}{\partial x_i}\right). \tag{6}$$

Given that the AMR is not spatially symmetric in the central axis, a three-dimensional computational fluid model of the flow field must be established. To reduce the calculation scale of the model, a quarter of the entire computational domain of the flow field is selected for modeling. The computational fluid dynamics model of aerostatic bearings is divided using the three-dimensional structured grid. The complex turbulent vortex structure mainly appears in the recess, while the air flow in the air film is in laminar flow state. Consequently, the laminar flow portion of the air film has a coarser mesh, whereas the orifice and recess use a refined grid. The grid resolution close to the wall is defined by the dimensionless distance $y^+ = \sqrt{\rho\tau_{\mathrm{w}}}y/u$ [30], which is maintained below 1. In this equation, τ_{w} symbolizes the shear stress on the wall, and y indicates the distance between the boundary and the centroid of the first grid layer close to the wall. The LES model is employed to accurately analyze the transient turbulent vortex structures, where the AMR and recess regions use the LES model, and the air film region uses a laminar flow model. The time step $\Delta t = 1 \times 10^{-8}$ s is determined based on the well-known Courant–Friedrichs–Lewy condition. A compressible air model is used for calculations, with the fluid (air) set as an ideal gas. At the inlet, a pressure inlet boundary condition is applied with a supply pressure (absolute) set to $P_{\mathrm{s}} = 0.4$ MPa. At the air film perimeter outlet, a pressure outlet boundary condition is used, with the pressure set to standard atmospheric pressure. The

solid walls are assigned no-slip and adiabatic boundary conditions. To eliminate the influence of mesh resolution on the computational results, a grid independence study is performed. When the total number of mesh elements reaches 2 million, the standard deviation of the LCC fluctuation remains essentially unchanged.

3 Results and discussion

3.1 Generation and evolution of vortices

To analyze the turbulent vortex generation process and evolution pattern of aerostatic bearings with AMRs, a detailed analysis of the airflow in the recess of a 4-orifice bearing is conducted, as shown in Fig. 2. When high-velocity, high-pressure gas enters the recess through the restrictors, rapid expansion occurs, which causes the main flow to detach from the upper wall of the recess. As a result, a separation zone A is formed. The air compression zone B is created when the high-velocity airflow hits the bottom wall of flow field perpendicularly, which continually compresses and builds up the air. The airflow channel C is created between the separation zone A and the compression zone B. When the high-speed airflow V_1 collides with the bottom wall and reflects to create airflow V_2, the collision of airflow V_2 with the upper wall of the recess leads to velocity separation, which forms airflows V_3 and V_4. Owing to the presence of channel C, the high-velocity airflow from the restrictor interacts with the surrounding airflows. These airflows then separate into different velocities and form velocity vortices. The airflows between neighboring restrictors exhibit opposite rotational directions, which lead to the creation of multiple multi-scale turbulent vortices as airflows with varying velocities and directions interact aggressively with the nearby air. These vortices induce significant pressure fluctuations in the recess, which result in bearing micro-vibrations. Based on the abovementioned analysis, decreasing the restrictor diameter and increasing the multi-orifice number while keeping the total orifice area unchanged can reduce the amount of air that accumulates at the bottom. This condition effectively controls the air separation phenomena in region A. It also eradicates the negative consequences of compression zone B, which inhibits the formation of turbulence vortices.

3.2 Steady flow field analysis

To investigate the static characteristics of bearings with AMRs, the steady-state flow field of the bearing is calculated. The pressure distribution and streamline contours at the symmetric cross section (diagonal line of red orifices in Fig. 1) of aerostatic bearings with 1-orifice, 4-orifice, 16-orifice (square), 16-orifice (circular), 36-orifice (square), and 36-orifice (circular) AMRs are shown in Fig. 3. A large-scale vortex exists near the upper wall area of the 1-orifice restrictor outlet, while smaller-scale vortices are present outside the 4-orifice restrictor outlets and between the orifices, with the vortices between the orifices being relatively smaller. The scale of vortices in the outer area of the 16-orifice (square) and 16-orifice (circular) AMRs is very small, and vortices in the outer area of the 36-orifice (square) and 36-orifice (circular) AMRs tend to disappear. The scale of vortices between the arrayed orifices also diminishes. The velocity distribution and streamline contours at the symmetric cross section of bearings with various orifice numbers are shown in Fig. 4. Near the outlet of the 1-orifice restrictor, the flow velocity increases, which leads to a significant pressure drop at this location. As the array number increases, the flow velocity in the area around the restrictor outlets becomes progressively smaller. When the array number is 16 or 36, bearings with circular AMRs exhibit lower flow velocity at the multi-orifice outlet compared with those with square AMRs.

The occurrence of vortex structure between neighboring orifices is caused by the intricate coupling effects between their airflow. The orifice diameter decreases with increasing number of orifices, which

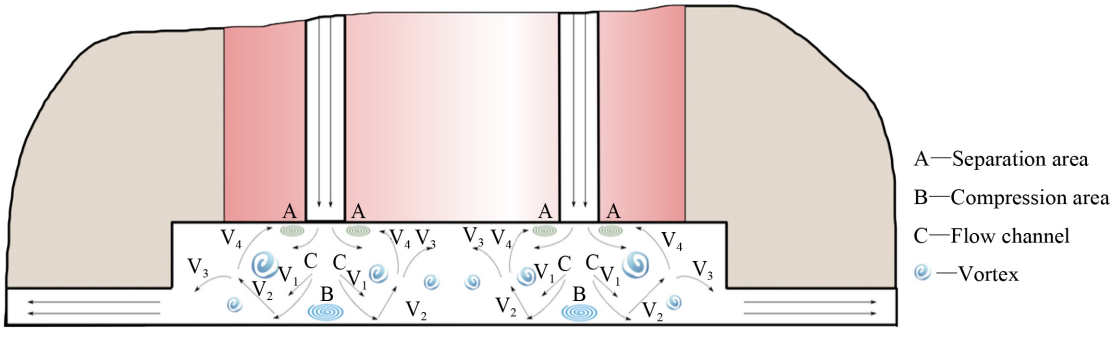

Fig. 2 Air flow model of aerostatic bearing with AMR.

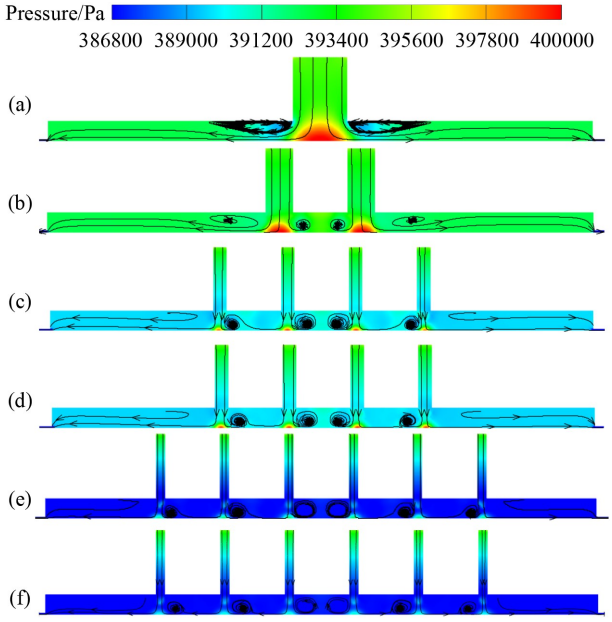

Fig. 3 One-dimensional pressure distributions of the aerostatic bearings with different orifice numbers (l = 0.3 mm). (a) 1-orifice; (b) 4-orifice; (c) 16-orifice (square); (d) 16-orifice (circular); (e) 36-orifice (square); (f) 36-orifice (circular).

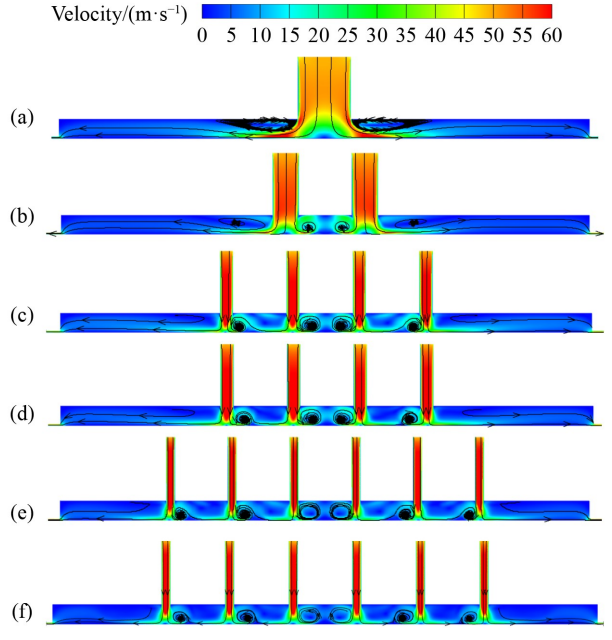

Fig. 4 One-dimensional velocity distributions of the aerostatic bearings with different orifice numbers (l = 0.3 mm). (a) 1-orifice; (b) 4-orifice; (c) 16-orifice (square); (d) 16-orifice (circular); (e) 36-orifice (square); (f) 36-orifice (circular).

decreases the airflow velocity at the orifice outlets. This decline results in fewer interactions between the airflow of nearby orifices, which reduces the quantity and strength of turbulent vortices.

The two-dimensional air film pressure distributions in the recess of bearings with 1-orifice, 4-orifice, 36-orifice (square), 16-orifice (square), and 16-orifice (circular) restrictors are shown in Fig. 5. Sharp pressure drops occur near the 1-orifice, 4-orifice, 16-orifice, and 36-orifice restrictors, with smaller pressure peaks between the orifices. However, the magnitude of pressure drops and rises near the orifices tends to level off when the number of orifices increases.

The one-dimensional pressure distributions of aerostatic bearings with 1-orifice, 4-orifice, 16-orifice (square), 16-orifice (circular), 36-orifice (square), and 36-orifice (circular) restrictors are shown in Fig. 6(a). The pressure distributions of aerostatic bearings with different restrictors are the same, except for the differences in the recess. The pressure fluctuation, which is denoted as $\Delta P = P_{\max} - P_{\min}$, represents the magnitude of pressure drop and rise near the orifices and is commonly employed to evaluate vortex energy [35]. In the calculation, the selected peak points of pressure rise and drop in the recess exclude those located directly at the orifices. The points corresponding to the maximum and minimum values of the pressure rise and drop in the recess are shown in Fig. 6(b). Among these bearings, the aerostatic bearing with 1-orifice restrictor exhibits the maximum pressure fluctuation with ΔP of approximately 2250 Pa. Meanwhile, the 36-orifice bearing with circular distribution shows the smallest fluctuation with ΔP of approximately 600 Pa. The pressure fluctuation in the

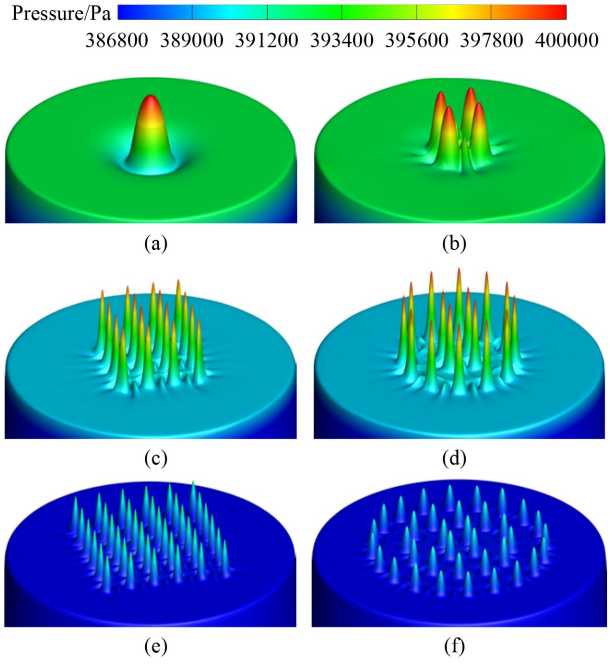

Fig. 5 Two-dimensional air film pressure distributions in the recess: (a) 1-orifice, (b) 4-orifice, (c) 16-orifice (square), (d) 16-orifice (circular), (e) 36-orifice (square), and (f) 36-orifice (circular) restrictors.

recess diminishes as the number of orifices increases, which indicates that a higher number of orifices result in smaller micro-vibrations in the bearing. The one-dimensional pressure distribution of 16-orifice aerostatic bearings with various orifice spacing is shown in Figs. 7 and 8. Overall, the pressure distributions of 16-orifice bearings with different orifice spacing are largely consistent. As the orifice spacing increases, the pressure peak shifts radially. For the 16-orifice bearing, regardless of whether the distribution is square or circular, larger orifice spacing leads to smaller pressure fluctuations in the recess. When the orifice spacing is the same, bearings with circular AMRs exhibit smaller pressure fluctuations than the bearings with square AMRs.

To compare the static performance of bearings with AMRs, the LCC and stiffness of bearings with 1-orifice, 4-orifice, 16-orifice (square), 16-orifice (circular), 36-orifice (square), and 36-orifice (circular) AMRs are calculated under different gas film thickness conditions, as shown in Fig. 9. For bearings with different orifice numbers, the trend of LCC variation with the gas film thickness is generally the same: it decreases as the film thickness increases. Under the same gas film thickness, the load capacity differences between bearings with different orifice numbers are minimal. The stiffness of bearings with 1-orifice, 4-orifice, 16-orifice (square), 16-orifice (circular), 36-orifice (square), and 36-orifice (circular) AMRs initially increases and then decreases as the gas film thickness rises. The stiffness of bearing with different restrictors shows minimal difference under the same conditions. Therefore, increasing the number of orifices has little effect on the LCC and stiffness of bearings when the entire restricted area remains constant.

3.3 Micro-vibration characteristics of bearings with various numbers and spacing of AMRs

To evaluate the effectiveness of the design of AMRs in suppressing micro-vibrations, the transient vortex

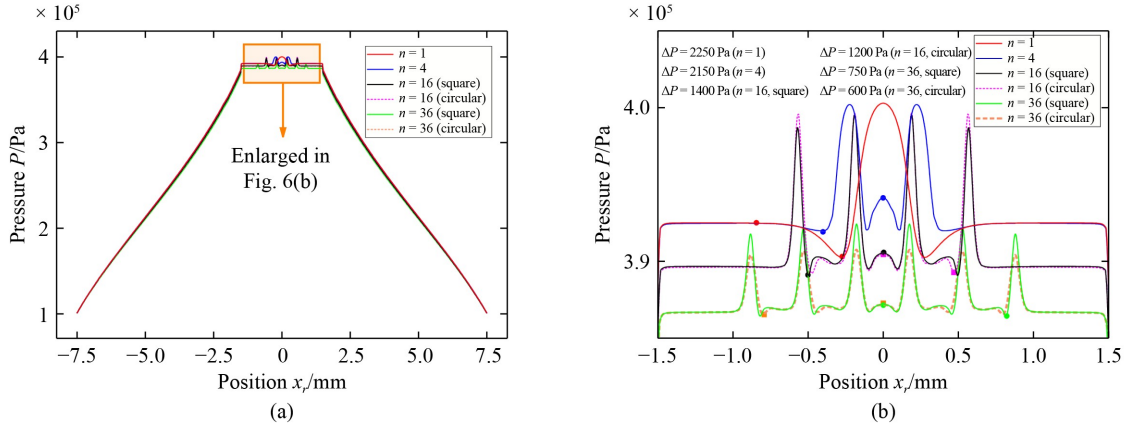

Fig. 6 One-dimensional radial pressure distribution of bearings with various orifice numbers (l = 0.3 mm). (a) Pressure distribution. (b) Local enlarged view of the pressure distribution.

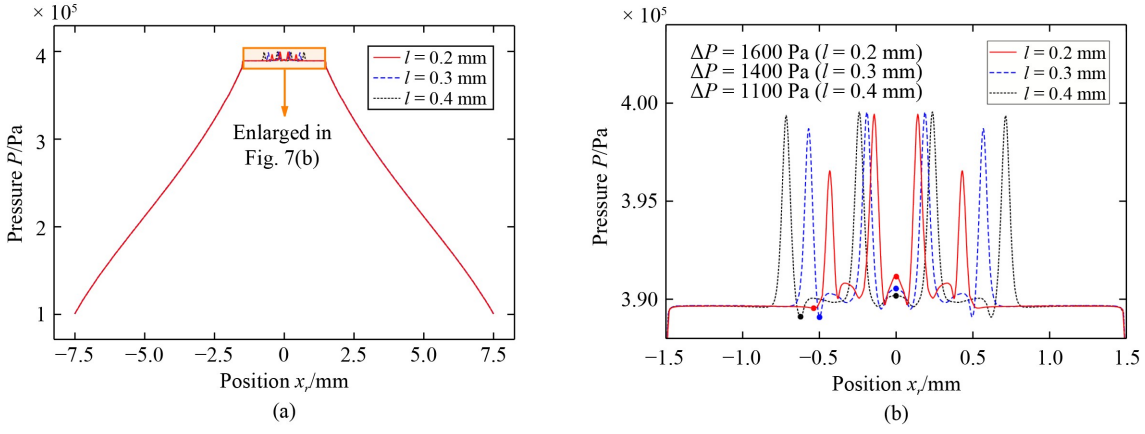

Fig. 7 One-dimensional radial pressure distribution of square distributed bearings with various spacing (n = 16). (a) Pressure distribution. (b) Local enlarged view of the pressure distribution.

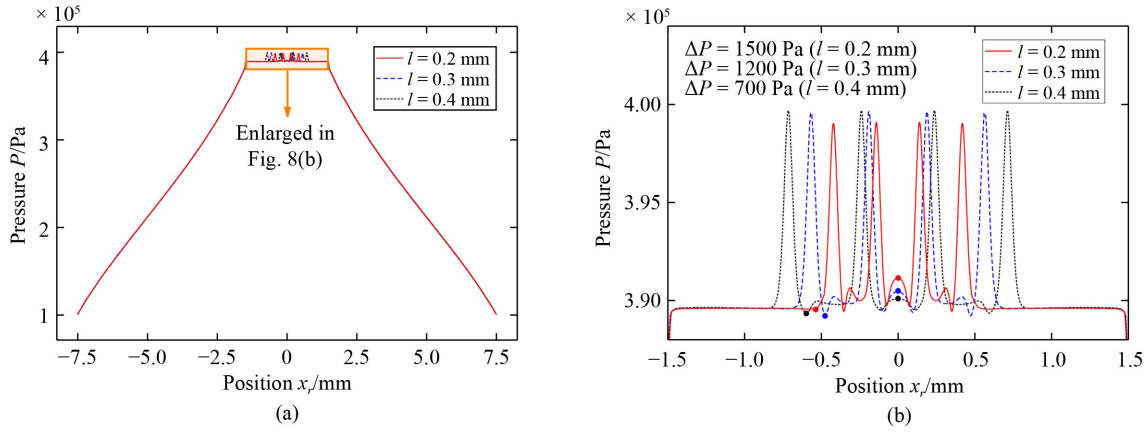

Fig. 8 One-dimensional radial pressure distribution of circular distributed bearings with various spacing ($n = 16$). (a) Pressure distribution. (b) Local enlarged view of the pressure distribution.

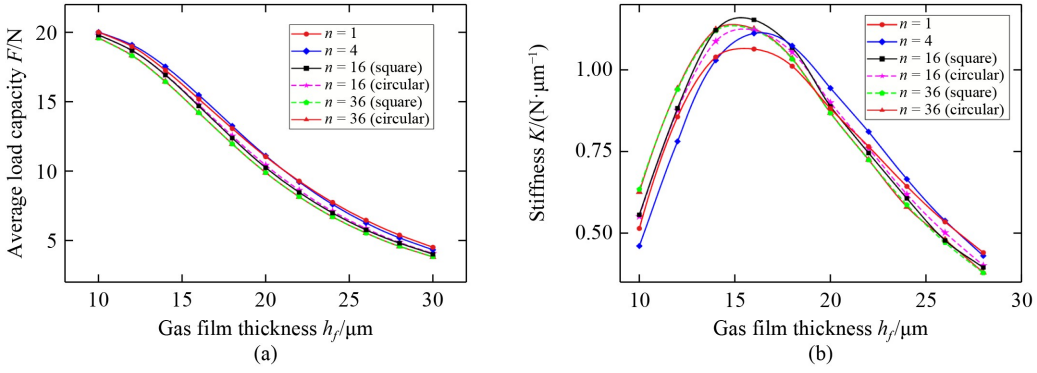

Fig. 9 Comparison of (a) LCC and (b) stiffness between the bearings with 1-orifice, 4-orifice, 16-orifice (square), 16-orifice (circular), 36-orifice (square), and 36-orifice (circular) restrictors.

shedding and pressure variations in the flow fields of bearings with various restrictors are analyzed and compared by three-dimensional LES. Figures 10(a) and 10(b) show transient pressure distribution in the recess of the bearing with 1 orifice and 36 orifices, respectively. The bearing gas film thickness is 10 μm. The pressure contour of the bearing with 1 orifice varies significantly with time, while the pressure contour of the bearing with 36 orifices changes little over time. As observed from the locally enlarged view of the 36-orifice bearing in Fig. 10(b), the pressure remains nearly constant over time near the orifice outlets and between adjacent orifices. By contrast, the pressure distribution near the orifice outlet of the 1-orifice bearing varies noticeably over time. Figures 11(a) and 11(b) show the instantaneous flow states at different moments in the recess of the aerostatic bearing with 1 and 36 orifices, respectively. To clearly demonstrate the scale and movement of the vortex structures, the streamline patterns and the positional change of local pressure drops accompanying the vortices are also observed. Overall, the streamlines bend sharply as the exit flow from the orifice vertically impinges on the lower wall of the recess. After entering the recess, the airflow gradually diffuses radially, and the vortex shedding phenomenon in the 1-orifice restrictor is quite pronounced. While vortex structures still exist between the arrayed orifices, the shape, position, and scale show minimal changes over time. Moreover, no significant vortex shedding is observed. For the aerostatic bearing with 36 orifices, only the vortex structure between the central orifices exhibits noticeable variation in size over time, while the vortices between the outer orifices remain nearly unchanged in size and position. In addition, no vortex shedding is observed outside the AMR, and the downstream flow is predominantly laminar.

The turbulent vortex structures with various orifice numbers are shown in Fig. 12. Color-filled contours of the vertical component of vorticity are used to visualize the rotational structures in the flow field. A large number of vortices with various shapes are generated near the restrictor outlet. When the high-velocity airflow enters the recess from the restrictor, it collides with the bottom surface. This collision

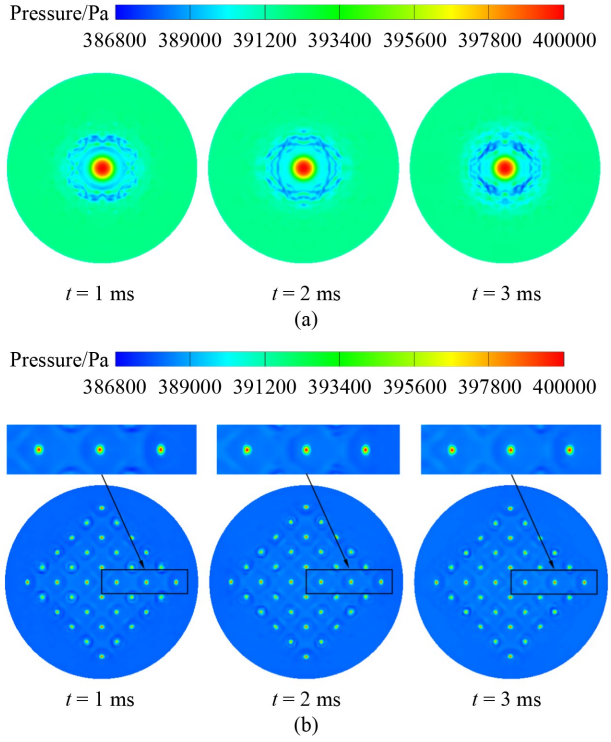

Fig. 10 Transient pressure distribution in the recess: (a) 1 orifice; (b) 36 orifices ($l = 0.4$ mm).

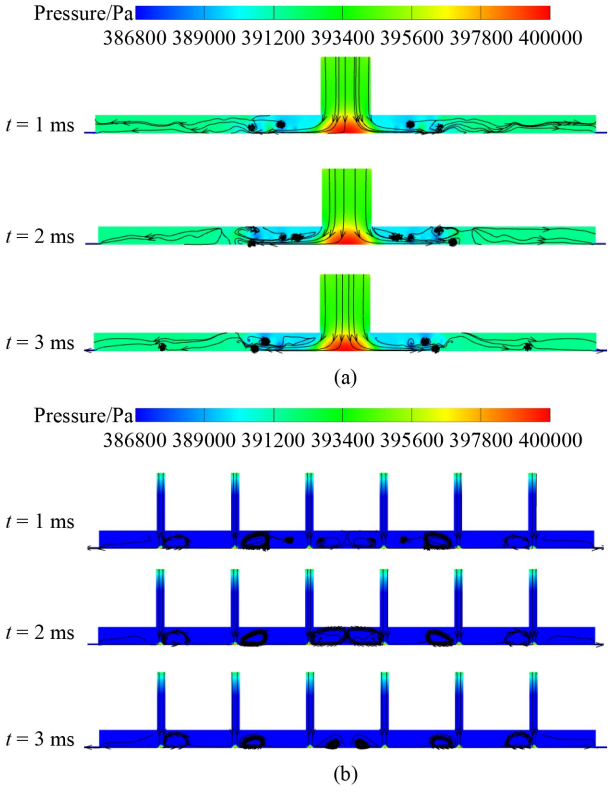

Fig. 11 Instantaneous flow states at different moments in the recess: (a) 1 orifice; (b) 36 orifices ($l = 0.4$ mm).

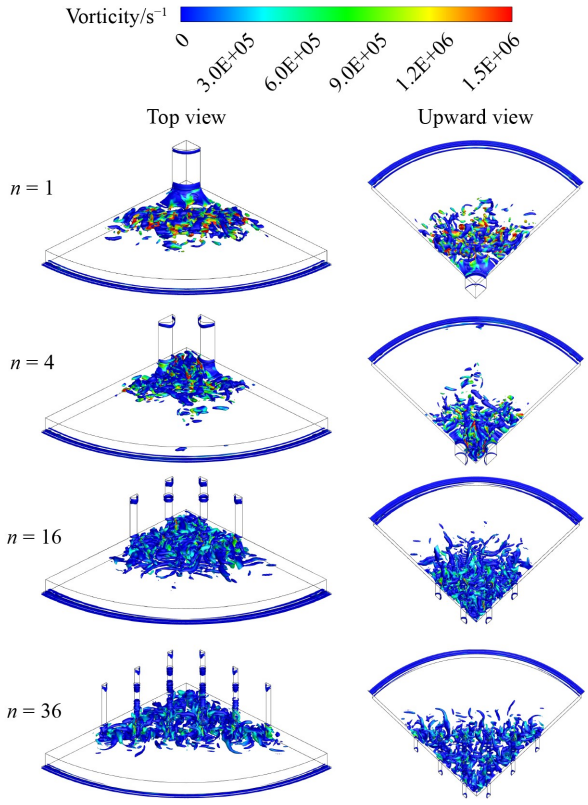

Fig. 12 Transient Q-criterion iso-surface in the recess with various orifice numbers ($l = 0.3$ mm).

causes the flow to sharply curve and then diffuse radially. Under the influence of the solid wall, the flow exhibits periodic upward and downward motions. It eventually dissipates due to the viscosity of the gas. The vorticity is maximized near the orifice exit of the 1-orifice aerostatic bearing. The dynamic and disordered vortex structures around the restrictor decrease when the orifice number rises. The vorticity and scale of the turbulent vortices in the AMR region also decrease progressively. The influence of orifice number and spacing on the pressure fluctuation ΔP and maximum vorticity magnitude in the recess is further analyzed. Table 2 presents the corresponding results. Under an orifice spacing of 0.3 mm, increasing the number of orifices from 1 to 36 leads to a reduction in pressure fluctuation ΔP from 2250 to 750 Pa. Meanwhile, the maximum vorticity magnitude decreases from 5.06×10^7 to 2.47×10^6 s^{-1}, which demonstrates a significant reduction in vortex intensity with the increase in orifice number.

Figure 13 shows the turbulent vortex structures with various orifice spacing ($n = 36$). The three-dimensional vortex structures are clearly visualized through the contour surfaces. This clear visualization allows easy capture of the detailed interactions between the airflow of neighboring orifices. The variation in array spacing significantly affects the vorticity

Table 2 Vortex intensity characteristics in recess with various numbers and spacing

Parameters		Pressure fluctuation ΔP/Pa	Maximum vorticity magnitude/s^{-1}
n	l/mm		
1	–	2250	5.06×10^7
4	0.3	2150	1.51×10^7
16	0.3	1400	1.42×10^7
36	0.2	810	2.49×10^6
36	0.3	750	2.47×10^6
36	0.4	630	2.41×10^6

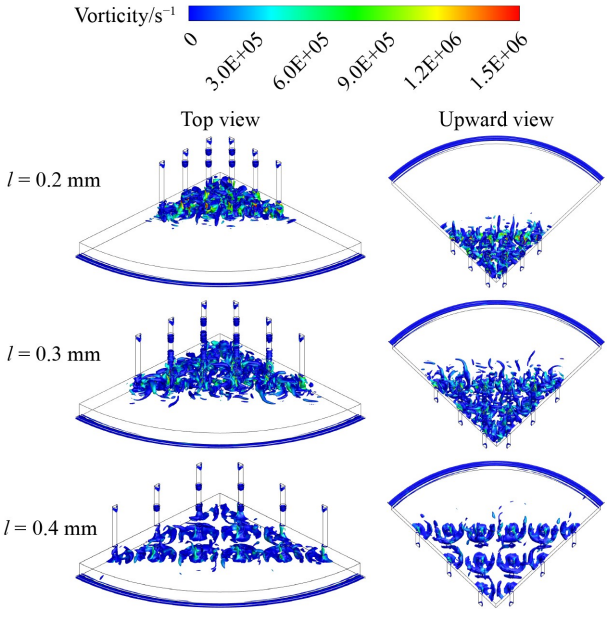

Fig. 13 Transient Q-criterion iso-surface in the recess with various array spacing ($n = 36$).

and complexity of the vortices. The vorticity is larger in the bearing flow field with a smaller array spacing, especially in the region among the array orifices where the turbulent vortices become more complex. The vortex structures downstream of the recess evolve toward a more ordered and stable state. According to the results in Table 2, when the number of orifices is fixed at 36, increasing the orifice spacing from 0.2 to 0.4 mm reduces the pressure fluctuation ΔP from 810 to 630 Pa. It also decreases the maximum vorticity magnitude from 2.49×10^6 to 2.41×10^6 s^{-1}. These results indicate that a larger orifice spacing can further suppress vortex intensity and enhance stability.

The performance of bearings with AMR, particularly the magnitude of micro-vibrations, is closely related to the design of the restrictors. The key factors affecting performance include the orifice diameter, array number, and array spacing. When the restricted area is kept constant, the orifice diameter is correlated with the number of orifices. The suppression of vortex shedding by the AMR will reduce pressure fluctuations in the entire air film. To facilitate comparison, the vibration magnitude of the bearing is assessed using LCC fluctuations. The time-varying LCC fluctuation curves of bearings with various array numbers are shown in Fig. 14, allowing for a quantitative analysis of the suppression effect of AMR on turbulent vortices. The amplitude of LCC fluctuations decreases when the number of orifices increases. Figure 15 shows the time-varying LCC fluctuation curves for bearings with different array spacing ($n = 16$). As the array spacing increases, the amplitude of LCC fluctuations in the aerostatic bearings decreases progressively.

Aerostatic bearings are extensively employed in ultra-precision machining equipment, such as H-type workbenches. During operation, the gas film thickness of the aerostatic bearing is approximately 10 μm, corresponding to a bearing capacity of 20 N, which equates to a load mass of 2 kg. The stiffness of bearings with 1, 4, 16, and 36 orifices ranges from a minimum of 0.46 N/μm to a maximum of 0.63 N/μm. The calculated natural frequency range of the aero-

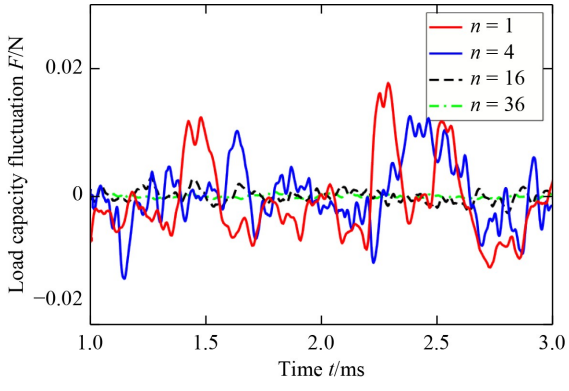

Fig. 14 LCC fluctuations of bearings with different array numbers ($l = 0.3$ mm).

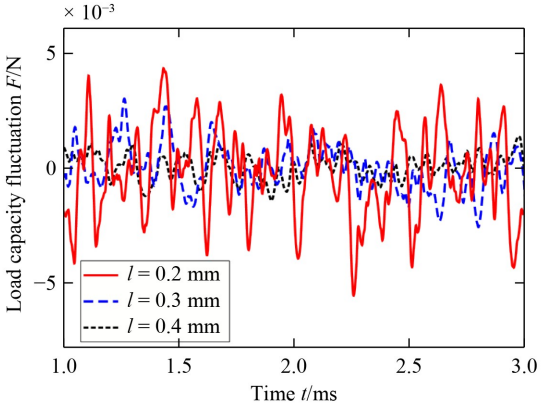

Fig. 15 LCC fluctuations of bearings with different array spacing ($n = 16$).

static bearing is 76.3–89.3 Hz. Given that the motion control of workbench is challenging in the 80–140 Hz range, fluctuations in the supporting force of the bearing significantly affect the motion stability of the workbench. The 1-orifice bearing exhibits the largest supporting force fluctuation, with a peak value of 0.017 N. For a load mass of 2 kg, this acceleration corresponds to a peak of 8.9×10^{-3} m/s^2. The 36-orifice bearing with an orifice spacing of 0.4 mm shows the smallest supporting force fluctuation, with a peak value of 4.4×10^{-4} N. For a load mass of 2 kg, the peak acceleration is 2.2×10^{-4} m/s^2, which gives a 97.5% reduction compared with the 1-orifice bearing.

The amplitude and standard deviation of LCC fluctuations under different array numbers and spacing, as obtained from numerical simulations, are shown in Figs. 16 and 17. Compared with using a 1-orifice restrictor, the pressure fluctuations and micro-vibrations of aerostatic bearings decrease progressively when using 4-orifice, 16-orifice, and 36-orifice AMRs. When comparing the amplitude of LCC fluctuations at different spacing, the fluctuation amplitude decreases as spacing increases. When the spacing is 0.4 mm, the load fluctuation reaches its minimum. Compared with the 1-orifice bearing, the LCC fluctuations amplitude of bearings is reduced by 36%, 89%, and 98% for the 4-orifice, 16-orifice, and 36-orifice configurations, respectively. The corresponding standard deviations are reduced by 48%, 90%, and 97%, and the peak-to-peak values are decreased by 27%, 88%, and 97%, respectively. This observation aligns with the downward trend in maximum vorticity magnitude presented in Table 2. In aerostatic bearings with a 4-orifice AMR, the reduction in LCC fluctuations is significant as the orifice spacing increases. By contrast, in those with a 36-orifice AMR, the reduction is relatively less pronounced. For the bearings with AMRs, as the spacing between the orifices decreases, vortex shedding becomes more pronounced, which results in larger pressure fluctuations. Chen et al. [36] experimentally measured the vibration acceleration of bearings with three different numbers of orifices. The amplitude of vibration acceleration in aerostatic bearings decreases progressively from 1-orifice restrictors to 4-orifice and 9-orifice restrictors. Compared with the 1-orifice configuration, the 4-orifice array reduces the amplitude by approximately 50%, while the 9-orifice array achieves a reduction of approximately 70%. The trend revealed by the numerical analysis in this study is consistent with their experimental results, which demonstrate that increasing the number of orifices can effectively suppress bearing vibrations, and the AMRs can effectively suppress the shedding of eddy currents and effectively suppress bearing vibrations.

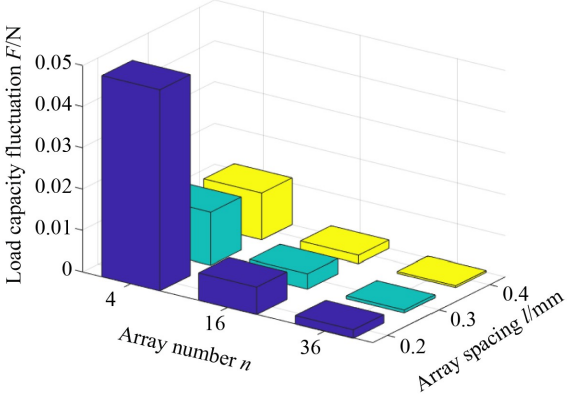

Fig. 16 LCC fluctuation amplitude of bearings.

3.4 Micro-vibration characteristics of bearings with various distribution types of AMRs

Increasing the array spacing can reduce micro-vibrations in aerostatic bearings. For the aerostatic bearings with square AMR, increasing the spacing between the orifices effectively reduces micro-vibrations. When the spacing is greater than 0.3 mm, the LCC fluctuations of aerostatic bearings with 16 and 36 orifices show minimal difference. Considering the superior manufacturing cost-effectiveness of the

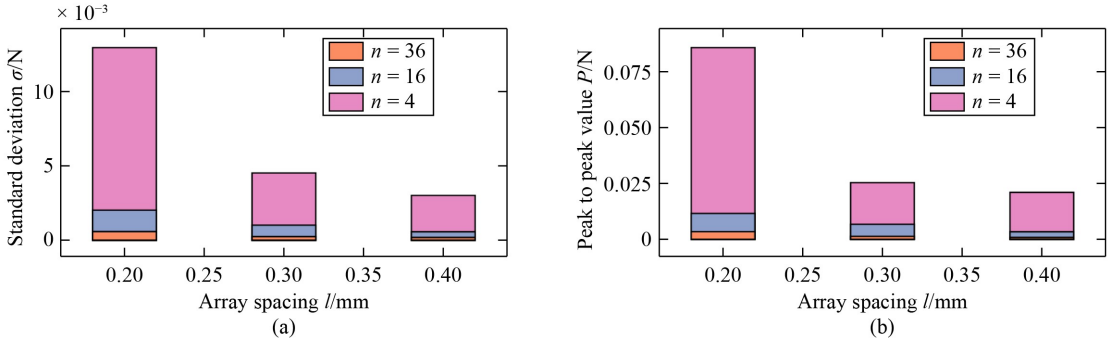

Fig. 17 LCC fluctuations of the bearings: (a) standard deviation and (b) peak-to-peak value.

16-orifice AMR to the 36-orifice AMR, the 16-orifice AMR is preferred in the optimization design of AMR. Therefore, this study investigates the impact of different distribution types of AMRs on the LCC fluctuations of the bearings with a 16-orifice AMR. Figure 18 shows the transient pressure distribution on the recess bottom wall of the 16-orifice aerostatic bearing with AMRs in square and circular distributions. As shown in Fig. 18(a), the transient pressure distribution on the recess bottom wall of the 16-orifice aerostatic bearing with AMRs in square distribution varies significantly with time. As shown in Fig. 18(b), the transient pressure distribution on the recess bottom wall of the 16-orifice aerostatic bearing with circular distribution is stable and barely varies with time.

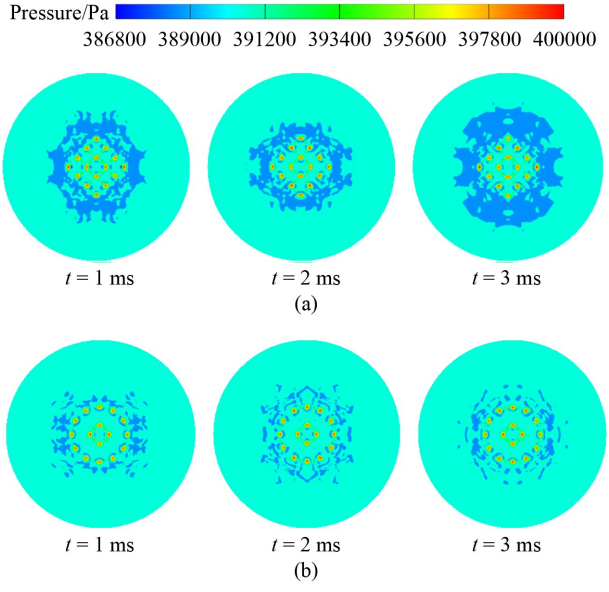

Fig. 18 Transient pressure distribution in the recess of bearings (l = 0.2 mm): (a) square distribution; (b) circular distribution.

Figure 19 shows the transient flow field at different times in the recess of the 16-orifice aerostatic bearing. It illustrates the streamline patterns and the positional change of local pressure drops associated with the appearance of vortices. Vortex structures exist between the arrayed orifices, with larger vortex scales between the inner orifices and smaller ones between the outer orifices. As shown in Fig. 19(a), in the recess of the bearing with square AMRs, the shape, position, and scale of the vortex structure change over time. These changes are accompanied by vortex shedding. By contrast, as shown in Fig. 19(b), in the recess of the bearing with circular AMRs, the vortex structure changes minimally over time with no significant vortex shedding observed. The downstream flow remains stable and orderly, with no vortex shedding occurring outside the orifices.

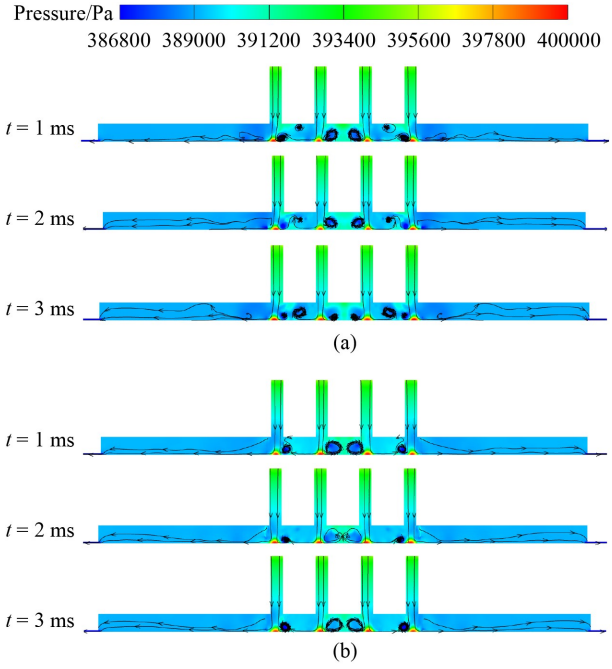

Fig. 19 Instantaneous flow states at different moments in the recess of bearings with 16 orifices (l = 0.2 mm): (a) square distribution; (b) circular distribution.

The flow field variations in aerostatic bearings are investigated using three-dimensional LES. Figure 20 shows turbulent vortex structure for 16-orifice aerostatic bearings with various array spacing in square and circular distribution. As shown in Fig. 20, compared with square distribution, aerostatic bearings with circular AMRs exhibit smaller vorticity near the restrictor outlets. The interactions between turbulent vortices among nearby orifices also decrease progressively, which leads to more stable and orderly vortex structures. Similarly, in square and circular distributions, the vorticity magnitude and complexity of turbulent vortices in the AMR region progressively diminish as the orifice spacing increases. The influence of the distribution type of AMRs on the pressure fluctuation ΔP and maximum vorticity magnitude in the recess is further analyzed. The corresponding results are presented in Table 3. When the number of orifices is fixed at 16 and the spacing increases from 0.2 to 0.4 mm, the pressure fluctuation ΔP of the bearing with square AMRs decreases from 1600 to 1100 Pa, and the maximum vorticity magnitude decreases from 1.48×10^7 to 1.40×10^7 s^{-1}. For the bearing with circular AMRs, the pressure fluctuation ΔP decreases from 1500 to 700 Pa, while the maximum vorticity magnitude decreases from 1.45×10^7 to 1.38×10^7 s^{-1}. At the same array spacing, the bearing with circular AMRs demonstrates smaller pressure fluctuation ΔP and weaker vortex intensity than the bearing with square AMRs.

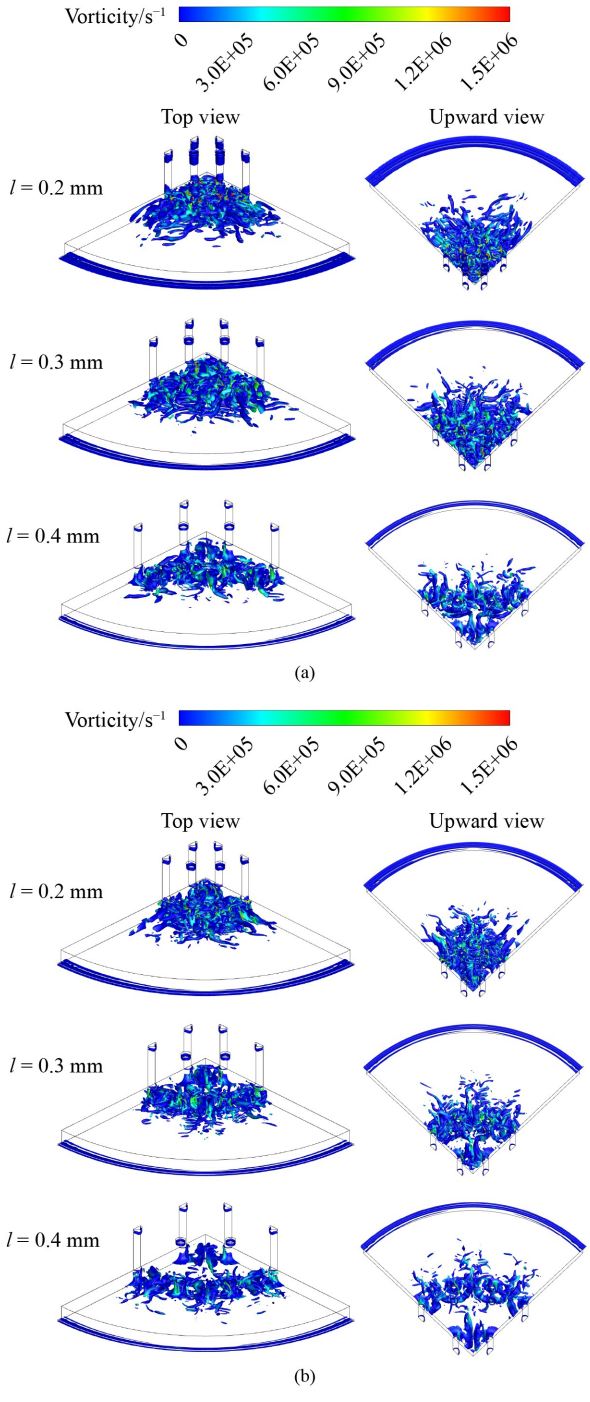

Fig. 20 Transient Q-criterion iso-surface in the recess with various distribution types. (a) Square distribution. (b) Circular distribution.

Figure 21 shows the LCC fluctuations of bearings with different distribution types ($n = 16$), and demonstrates that at the same array spacing, the amplitude of LCC fluctuations in circular distribution is smaller than in square distribution. In addition, as the array spacing becomes wider, the difference in LCC fluctuation amplitudes between circular and square distributions diminishes. As shown in Fig. 22,

Table 3 Vortex intensity characteristics in recess with various distribution types ($n = 16$)

Parameters		Pressure fluctuation ΔP/Pa	Maximum vorticity magnitude/s^{-1}
Type	l/mm		
Square	0.2	1600	1.48×10^7
Square	0.3	1400	1.42×10^7
Square	0.4	1100	1.40×10^7
Circular	0.2	1500	1.45×10^7
Circular	0.3	1200	1.41×10^7
Circular	0.4	700	1.38×10^7

compared with the bearing with a square distribution ($n = 16$), the bearings with a circular distribution exhibit reductions in the amplitude of LCC fluctuation by 60% ($l = 0.2$ mm), 54% ($l = 0.3$ mm), and 28% ($l = 0.4$ mm). The corresponding standard deviations are reduced by 55%, 48%, and 18%, and the peak-to-peak values are decreased by 56%, 53%, and 31%. At the same orifice spacing, the LCC fluctuations of bearings with circular AMRs are smaller than those of the bearings with square AMRs. Moreover, the fluctuations decrease as the orifice spacing increases. This trend is attributed to the more evenly distributed orifices in the circular distribution, which leads to smaller airflow disturbances between the orifices. This condition reduces the LCC fluctuations in the aerostatic bearings.

4 Conclusions

Improving the stability of aerostatic bearings without compromising static performance has always been a key challenge. This study presents an innovative aerostatic bearing design with square or circular AMRs to limit the generation of turbulence and diminish micro-vibrations. In accordance with turbulence vortex generation mechanisms, this study investigates the effect of array number, spacing, and distribution type on static and dynamic performance of the bearings with AMRs. The numerical results of pressure distribution, air velocity, and the static characteristics of aerostatic bearing with 1-orifice restrictor and AMRs are compared and analyzed. The three-dimensional LES is utilized to assess the pressure fluctuations and dynamic airflow behavior in the bearings. The findings clarify the effects of orifice configuration on vortex suppression, micro-vibrations, and bearing stability.

The aerostatic bearings with square or circular AMR may efficiently minimize the pressure fluctuation in the flow field, decrease the micro-vibration, and improve the stability of bearing. Varying the array number, spacing, and distribution type has

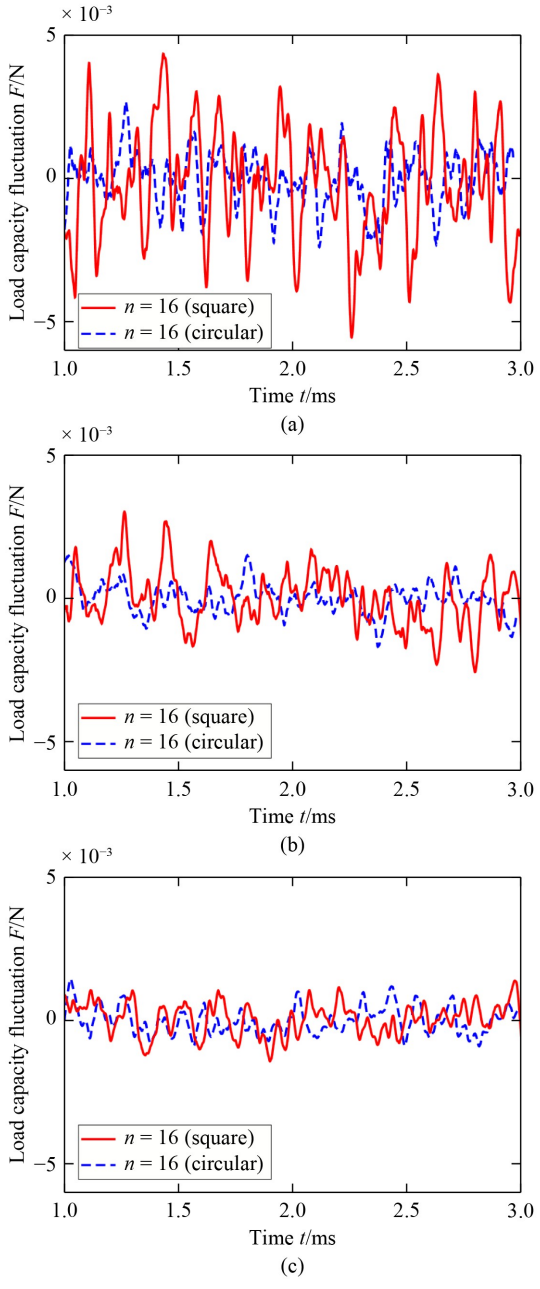

Fig. 21 LCC fluctuations of bearings with square and circular distribution (n = 16). (a) l = 0.2 mm. (b) l = 0.3 mm. (c) l = 0.4 mm.

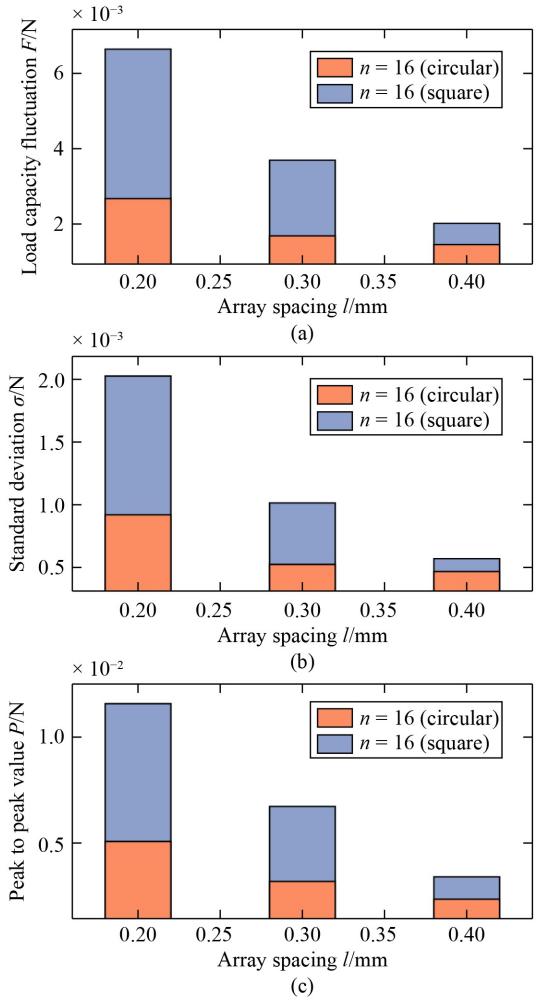

Fig. 22 LCC fluctuations of bearings with square and circular distribution (n = 16): (a) amplitude; (b) standard deviation; (c) peak to peak value.

minimal influence on the LCC and stiffness of the aerostatic bearing with AMRs as the entire restrictor region remains constant. This minimal influence suggests that the stability of bearings can be enhanced without compromising the LCC or stiffness. Increasing the array number can suppress turbulence generation near the restrictor, which significantly reduces the micro-vibrations of bearings. Expanding the spacing between orifices reduces airflow interactions, which mitigates turbulent vortex formation. The LCC fluctuations of bearings with AMRs consistently decrease as the array number and array spacing increase. However, when the array number reaches 16, the reduction in micro-vibrations levels off. For the 16-orifice bearing with a square distribution at l = 0.4 mm, the standard deviation of the LCC is reduced to one-tenth of that of the 1-orifice bearing. In contrast to the 1-orifice bearing, the LCC fluctuations of the bearing with square AMRs are reduced by over 97% when the array number is increased to 36 and the spacing to 0.4 mm.

For the same array number, the bearing with a circular distribution exhibits smaller micro-vibrations than that with a square distribution. When the array spacing is less than 0.3 mm, the LCC fluctuations of the 16-orifice bearing with a circular distribution are reduced by approximately 50% compared with those with a square distribution, which indicates a significant improvement. Therefore, in the optimization design of AMRs, a circular distribution with larger spacing should be used to effectively reduce micro-

vibrations. From a cost-effectiveness perspective, a 16-orifice circular distribution with larger spacing is recommended as the preferred restrictor configuration.

Nomenclature

Abbreviations

AMR	Arrayed multi-orifice restrictor
LCC	Load-carrying capacity
LES	Large eddy simulation
N-S	Navier–Stokes
SGS	Subgrid-scale

Acknowledgements This work was supported by the National Natural Science Foundation of China (Grant Nos. 52450241, 52305107, 52441505, 52275112, and 52075193) and the Major Program (JD) of Hubei Province, China (Grant No. 2025BEA006).

Conflict of Interest Xuedong CHEN is a member of the Editorial Board of *Frontiers of Mechanical Engineering* and was therefore excluded from the peer review and all editorial decisions related to the acceptance and publication of this article. Peer review was handled independently by other editors to minimize potential bias.

References

1. Li J S, Li X Z, Wei W, Liu P K. Relative vibration identification of cutter and workpiece based on improved bidimensional empirical mode decomposition. Frontiers of Mechanical Engineering, 2020, 15(2): 227–239
2. Zheng L, Li J, Sun Y Z, Chen W Q, Zhang X. Design, analysis, and implementation of a compound restrictor aerostatic bearing system. Tribology International, 2025, 204: 110489
3. Dal A, Karaçay T. Effects of angular misalignment on the performance of rotor-bearing systems supported by externally pressurized air bearing. Tribology International, 2017, 111: 276–288
4. Qiu S, Ke C L, Li K R, Zhang X H, Peng N, Liu L Q. Nonlinear dynamic analysis of a novel tangentially supplied aerostatic bearing-rotor system: Theory and experiment. Mechanical Systems and Signal Processing, 2025, 224: 112221
5. Wang X K, Xu Q, Wang B R, Zhang L X, Yang H, Peng Z K. Effect of surface waviness on the static performance of aerostatic journal bearings. Tribology International, 2016, 103: 394–405
6. Cheng C, Zhao M, Zhao Z H, Liu Z X, Hou W J, Yan L J, Li Z X, Chen S, Xu L C. Study on micro-vibration mechanism and flow characteristics of aerostatic bearings based on proper orthogonal decomposition. Physics of Fluids, 2024, 36(8): 087104
7. Luo X H, Han B, Chen X D, Li X P, Jiang W. Multi-physics modeling of tunable aerostatic bearing with air gap shape compensation. Tribology International, 2021, 153: 106587
8. Maamari N, Krebs A, Weikert S, Wild H, Wegener K. Stability and dynamics of an orifice based aerostatic bearing with a compliant back plate. Tribology International, 2019, 138: 279–296
9. Sahto M P, Wang W, Imran M, He L S, Li H, Gong W W. Modelling and simulation of aerostatic thrust bearings. IEEE Access, 2020, 8: 121299–121310
10. Wu Y K, Li C L, Li J, Du J J. Lubrication mechanism and characteristics of aerostatic bearing with close-spaced micro holes. Tribology International, 2024, 192: 109278
11. Liang C Y, Yuan F, Chen X D, Jiang W, Zeng L Z, Luo X. Comprehensive analysis of the influence of structural and dynamic parameters on the accuracy of nano-precision positioning stages. Frontiers of Mechanical Engineering, 2019, 14(3): 255–272
12. Feng K, Li J, Li W J, Huang J F, Gao F W, Sun J Y. A novel parallel capillary-cavity model for the analysis of pneumatic hammer vibration in porous aerostatic bearings. Tribology International, 2023, 189: 108993
13. Miettinen M, Vainio V, Viitala R. Aerostatic porous annular thrust bearings as seals. Tribology International, 2024, 200: 110073
14. Vainio V, Miettinen M, Majuri J, Theska R, Viitala R. Manufacturing and static performance of porous aerostatic bearings. Precision Engineering, 2023, 84: 177–190
15. Miettinen M, Vainio V, Theska R, Viitala R. On the static performance of aerostatic elements. Precision Engineering, 2024, 89: 1–10
16. Zeng C Q, Wang W, Cheng X H, Zhao R, Cui H L. Three-dimensional flow state analysis of microstructures of porous graphite restrictor in aerostatic bearings. Tribology International, 2021, 159: 106955
17. Li W J, Wang S J, Feng K. Numerical and experimental study on the effect of surface damages on the performances of porous aerostatic bearings.

Tribology International, 2022, 175: 107791
18. Li Y F, Yin Y H, Yang H, Liu X E, Mo J, Cui H L. Micro-vibration analysis and optimization of aerostatic bearing with pocketed orifice-type restrictor. Journal of Applied Fluid Mechanics, 2018, 11(4): 1115–1124
19. Wang G Q, Li W J, Liu G P, Feng K. A novel optimization design method for obtaining high-performance micro-hole aerostatic bearings with experimental validation. Tribology International, 2023, 185: 108542
20. Boffey D A, Duncan A E, Dearden J K. An experimental investigation of the effect of orifice restrictor size on the stiffness of an industrial air lubricated thrust bearing. Tribology International, 1981, 14(5): 287–291
21. Boffey D A, Barrow A A, Dearden J K. Experimental investigation into the performance of an aerostatic industrial thrust bearing. Tribology International, 1985, 18(3): 165–168
22. Li Y T, Ding H. A simplified calculation method on the performance analysis of aerostatic thrust bearing with multiple pocketed orifice-type restrictors. Tribology International, 2012, 56: 66–71
23. Charki A, Diop K, Champmartin S, Ambari A. Numerical simulation and experimental study of thrust air bearings with multiple orifices. International Journal of Mechanical Sciences, 2013, 72: 28–38
24. Wen Z P, Wu J W, Tan J B. An adaptive modeling method for multi-throttle aerostatic thrust bearing. Tribology International, 2020, 149: 105830
25. Wang P, Chen B, Li J, Wang J W, Zhang Y J, Feng K. Novel aerostatic bearings with hermetically squeeze film dampers for the improvement of stability: Theoretical and experimental investigations. Precision Engineering, 2024, 85: 263–278
26. Wang P, Zhang Y J, Feng L B, Hou W J, Wang J W, Li W J, Feng K. Study on the pneumatic hammer phenomenon of aerostatic bearings based on the empirical mode method: Numerical and experimental analysis. Tribology International, 2023, 181: 108305
27. Zhou Y J, Chen X D, Chen H. A hybrid approach to the numerical solution of air flow field in aerostatic thrust bearings. Tribology International, 2016, 102: 444–453
28. Li Y T, Ding H. Influences of the geometrical parameters of aerostatic thrust bearing with pocketed orifice -type restrictor on its performance. Tribology International, 2007, 40(7): 1120–1126
29. Du J J, Zhang G Q, Liu T, To S. Improvement on load performance of externally pressurized gas journal bearings by opening pressure-equalizing grooves. Tribology International, 2014, 73: 156–166
30. Zheng Y Q, Yang G W, Cui H L, Hou Y. Improving the stiffness of the aerostatic thrust bearing by using a restrictor with multi-orifice series. Proceedings of the Institution of Mechanical Engineers, Part J: Journal of Engineering Tribology, 2020, 234(12): 1881–1891
31. Chen X D, He X M. The effect of the recess shape on performance analysis of the gas-lubricated bearing in optical lithography. Tribology International, 2006, 39(11): 1336–1341
32. Zhu J C, Chen H, Chen X D. Large eddy simulation of vortex shedding and pressure fluctuation in aerostatic bearings. Journal of Fluids and Structures, 2013, 40: 42–51
33. Aoyama T, Kakinuma Y, Kobayashi Y. Numerical and experimental analysis for the small vibration of aerostatic guideways. CIRP Annals, 2006, 55(1): 419–422
34. Ma W, Cui J W, Liu Y M, Tan J B. Improving the pneumatic hammer stability of aerostatic thrust bearing with recess using damping orifices. Tribology International, 2016, 103: 281–288
35. Aoyama T, Koizumi K, Kakinuma Y, Kobayashi Y. Numerical and experimental analysis of transient state micro-bounce of aerostatic guideways caused by small pores. CIRP Annals, 2009, 58(1): 367–370
36. Chen X D, Chen H, Zhu J C, Jiang W. Vortex suppression and nano-vibration reduction of aerostatic bearings by arrayed microhole restrictors. Journal of Vibration and Control, 2017, 23(5): 842–852
37. Feng K, Wang P, Zhang Y J, Hou W J, Li W, Wang J W, Cui H L. Novel 3-D printed aerostatic bearings for the improvement of stability: Theoretical predictions and experimental measurements. Tribology International, 2021, 163: 107149
38. Li W J, Wang G Q, Feng K, Zhang Y C, Wang P. CFD-based investigation and experimental study on the performances of novel back-flow channel aerostatic bearings. Tribology International, 2022, 165: 107319
39. Li W J, Zhang Y C, Cai S L, Lei X P, Feng K. Numerical and experimental investigation on the performance of backflow channel aerostatic bearings with shunt injection. Tribology Transactions, 2023, 66(2): 193–207
40. Yu P L, Huang L, Li S Z, Guo L B, Zhong M, Zhang L P. Theoretical predictions and experimental measurements of novel aerostatic bearing with multi-inclined-orifice restrictors for the improvement of stability. Precision Engineering, 2024, 88: 266–278
41. Zhao M, Zhao Z H, Cheng C, Liu Z X, Hou W J, Yan L J, Li Z X, Chen S, Xu L C. Proper orthogonal decomposition analysis of flow characteristics of aerostatic bearings based on Large Eddy Simulation. Aerospace Science and Technology, 2024, 153: 109438
42. Li W J, Cai S L, Zhang P F, Ping Y, Feng K. Numerical and experimental study on the novel active aerostatic bearings with the controllable throttling effect for obtaining high static stiffness. Mechanical Systems and Signal Processing, 2024, 216: 111469
43. Yu P L, Zuo T, Lu J, Zhong M, Zhang L P. Static and dynamic performances of novel aerostatic bearings with primary and secondary orifice restrictors. Lubricants, 2023, 11(12): 518